NANO · MICRO small
www.small-journal.com

Ultrathin In_2O_3 Nanosheets toward High Responsivity and Rejection Ratio Visible-Blind UV Photodetection

Mingxi Zhang, Huan Yu, Hang Li, Yan Jiang, Lihang Qu, Yunxia Wang, Feng Gao, and Wei Feng**

Photoelectrochemical-type visible-blind ultraviolet photodetectors (PEC VBUV PDs) have gained ever-growing attention due to their simple fabrication processes, uncomplicated packaging technology, and high sensitivity. However, it is still challenging to achieve high-performance PEC VBUV PDs based on a single material with good spectral selectivity. Here, it is demonstrated that individual ultrathin indium oxide (In_2O_3) nanosheets (NSs) are suitable for designing high-performance PEC VBUV PDs with high responsivity and UV/visible rejection ratio for the first time. In_2O_3 NSs PEC PDs show excellent UV photodetection capability with an ultrahigh photoresponsivity of 172.36 mA W^{-1} and a high specific detectivity of 4.43×10^{11} Jones under 254 nm irradiation, which originates from the smaller charge transfer resistance (R_{ct}) at the In_2O_3 NSs/electrolyte interface. The light absorption of In_2O_3 NSs takes a blueshift due to the quantum confinement effect, granting good spectral selectivity for visible-blind detection. The UV/visible rejection ratio of In_2O_3 NSs PEC PDs is 1567, which is 30 times higher than that of In_2O_3 nanoparticles (NPs) and exceeds all recently reported PEC VBUV PDs. Moreover, In_2O_3 NSs PEC PDs show good stability and good underwater imaging capability. The results verify that ultrathin In_2O_3 NSs have potential in underwater optoelectronic devices.

1. Introduction

Visible-blind ultraviolet photodetectors (VBUV PDs), converting UV signals into electrical signals, are the fundamental building blocks for sensing, space exploration, and communications.[1–7] Although conventional solid-state VBUV PDs have been widely investigated based on various wide-bandgap nanomaterials,[8–10] photoelectrochemical-type (PEC) VBUV PDs have attracted ever-growing attention due to their simple fabrication process, low-cost, high sensitivity, and potential applications in underwater optical communication.[11,12] Various wide-bandgap materials with different nanostructures have been designed for PEC VBUV PDs,[13–16] but single material-based PEC PDs usually show relatively poor photoresponse.[15,16] Some strategies have been developed for optimizing the performance of PEC VBUV PDs, such as coating heavy metal nanoparticles[17,18] and building heterojunctions,[19,20] and they inevitably increase complexity and cost. Therefore, it is important to explore more wide-bandgap semiconductors with good optical and electrical properties for building high-performance PEC VBUV PDs.

In_2O_3 is an important n-type semiconductor with great potential in UV optoelectronic devices due to its suitable bandgap,[21,22] good optical and electrical properties,[23] and good stability.[24] In_2O_3 nanostructure-based conventional solid-state UV PDs show good UV photoresponse, demonstrating their great potential application in UV PDs.[21,25] Recently, our group demonstrated the potential of In_2O_3 microrods in PEC UV PDs with high responsivity and good stability.[26] However, the spectral selectivity of In_2O_3-based UV PDs should be further improved due to most reported In_2O_3-based UV PDs having a bandgap in the range of 2.6–2.8 eV.[21,25,26] Labram et al. demonstrated that ultrathin In_2O_3 films showed a wider bandgap as the thickness decreased to less than 5 nm due to the quantum effect.[27] Therefore, it is of great significance to investigate In_2O_3 with a wider bandgap for designing PEC VBUV PDs with good spectral sensitivity.

In this work, we investigated the photoresponse of ultrathin In_2O_3 NSs and In_2O_3 NPs-based PEC VBUV PDs. In_2O_3 NSs were synthesized by a hydrothermal method with annealing[28] and In_2O_3 NPs were commercial samples. In_2O_3 NSs show

M. Zhang, H. Yu, L. Qu, Y. Wang, W. Feng
College of Chemistry
Chemical Engineering and Resource Utilization
Northeast Forestry University
Harbin 150040, China
E-mail: wfeng@nefu.edu.cn

H. Li
Key Laboratory of Engineering Bionics
Ministry of Education
Jilin University
Changchun 130022, China

H. Li
Changchun Institute of Optics
Fine Mechanics and Physics
Chinese Academy of Sciences
Changchun 130022, China

Y. Jiang, F. Gao
Key Laboratory for Photonic and Electronic Bandgap Materials
Ministry of Education
School of Physics and Electronic Engineering
Harbin Normal University
Harbin 150025, China
E-mail: gaofeng@hrbnu.edu.com

The ORCID identification number(s) for the author(s) of this article can be found under https://doi.org/10.1002/smll.202205623.

DOI: 10.1002/smll.202205623

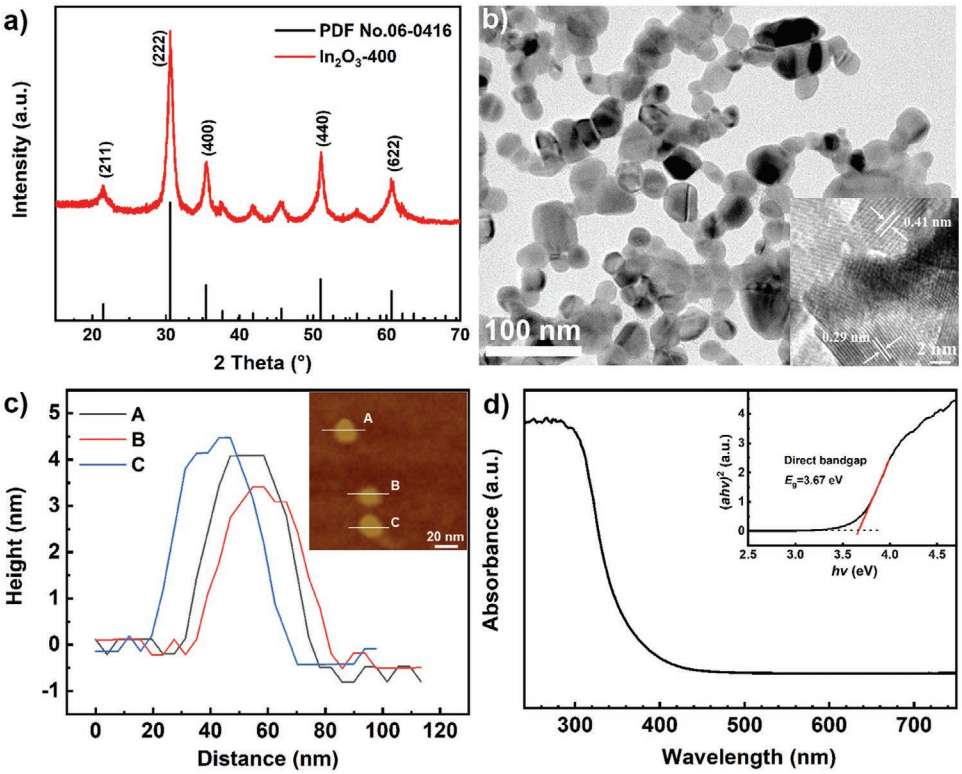

Figure 1. Characterization of ultrathin In_2O_3 NSs. a) XRD patterns. b) TEM images. Inset: corresponding HRTEM image. c) Height profiles. Inset: corresponding AFM image. d) UV–vis absorption spectra. Inset: corresponding Tauc curve of ultrathin In_2O_3 NSs as direct bandgap semiconductors.

ultrathin features with thicknesses in the range of 3.5–4.5 nm, while the size of commercial In_2O_3 NPs is ≈40–60 nm. Compared with In_2O_3 NPs, the light absorption of ultrathin In_2O_3 NSs shifts to the visible-blind region due to the quantum confinement effect.[27] In_2O_3 NSs-based PEC UV PDs show ultrahigh responsivity of 172.36 mA W^{-1} and excellent specific detectivity of 4.43×10^{11} Jones under 254 nm illumination at a bias voltage of 0.4 V, respectively, surpassing all reported ultrathin nanomaterial-based PEC UV PDs. The excellent UV photoresponse is attributed to the smaller R_{ct} between In_2O_3 NSs and electrolyte. Moreover, the In_2O_3 NSs-based PEC VBUV PDs reveal good wavelength selectivity for visible-blind detection. The UV–visible rejection ratio R_{254}/R_{455} is 1567, which is ≈30 times higher than that of In_2O_3 NPs and exceeds all recently reported PEC VBUV PDs. Moreover, ultrathin In_2O_3 NSs PEC PDs show good multicycle and long-term stability for 254 nm irradiation. Further, In_2O_3 NSs PEC PDs exhibit good underwater imaging capability.

2. Results and Discussion

2.1. Characterizations of In_2O_3 NSs

In_2O_3 NSs were synthesized by following an earlier report[28] (more details in Supporting Information). **Figure 1**a shows the X-ray diffraction (XRD) patterns of the synthesized samples. All the peaks are in accordance with the standard card (PDF No.06-0416) and can be indexed to the characteristic peaks of the cubic In_2O_3 sample.[28] No other impure diffraction peaks are observed, indicating good purity. The morphology of the synthesized In_2O_3 samples was observed by transmission electron microscopy (TEM). The synthesized In_2O_3 samples show a typical nanosheet morphology with lateral sizes in the range of 20–40 nm (Figure 1b and Figure S1a, Supporting Information). Figure 1b inset is the high-resolution TEM (HRTEM) image of In_2O_3 NSs, which further demonstrates its good crystallinity. The lattice spacings of the fringe pattern are 0.29 and 0.41 nm, corresponding to the (222) and (211) planes of the cubic In_2O_3 crystal, respectively, which are consistent with an earlier report.[28] All Raman peaks correspond to characteristic peaks of In_2O_3 (Figure S1b, Supporting Information), further demonstrating the successful preparation of the In_2O_3 sample. Atomic force microscopy (AFM) confirms that the thickness of In_2O_3 NSs is ≈3.5–4.5 nm, as shown in Figure 1c, demonstrating their ultrathin feature. The morphology of the commercial In_2O_3 NPs was observed by scanning electron microscopy (SEM), and the sizes of the In_2O_3 NPs are in the range of 40–60 nm, as shown in Figure S2, Supporting Information. The light absorption properties of In_2O_3 NSs and NPs were measured by UV–vis diffuse reflectance spectroscopy (Figure 1d and Figure S3, Supporting Information). Ultrathin In_2O_3 NSs have strong UV absorption, indicating their visible-blind photoresponse capability. Compared with commercial In_2O_3 NPs, the light absorption of ultrathin In_2O_3 NSs shifts to the visible-blind region, as shown in Figure 1d and Figure S3a, Supporting Information.

The blueshift of light absorption is attributed to the quantum confinement effect of ultrathin In_2O_3 NSs.[27] Due to the optical bandgap of In_2O_3 is under debate (direct or indirect bandgap), both direct and indirect optical bandgaps of In_2O_3 NSs are calculated by the Tauc curve using the equation of $(\alpha h\nu)^{1/n} = B \times (h\nu - E_g)$, where n values are 0.5 and 2 for direct bandgap and indirect bandgap semiconductor, α, $h\nu$, B, and E_g refer to the light absorption coefficient, energy of the photon, constant, and bandgap of ultrathin In_2O_3 NSs, respectively. The direct optical bandgap of ultrathin In_2O_3 NSs is 3.67 eV calculated by Tauc curves, as shown in Figure 1d inset, which is larger than that of commercial In_2O_3 NPs in Figure S3b, Supporting Information. Meanwhile, the indirect optical bandgap of ultrathin In_2O_3 NSs is also larger than that of commercial In_2O_3 NPs in Figure S3b,c, Supporting Information, further demonstrating their potential in visible-blind detection.

2.2. Photoresponse of Ultrathin In_2O_3 NSs PEC PDs

To investigate the photoresponse of ultrathin In_2O_3 NSs photoanodes (more details in the Experimental Section), a standard three-electrode system was designed, including working electrode (In_2O_3 NSs photoanodes, Figure S4, Supporting Information), reference electrode (Ag/AgCl), and counter electrode (Pt wire). The photoresponse of In_2O_3 NSs PEC PDs was recorded by an electrochemical workstation (**Scheme 1**). There is a built-in electric field pointing from n-type In_2O_3 to electrolytes after the In_2O_3 NSs photoanodes immersion in the solution.[26] The photogenerated electrons flow from In_2O_3 to FTO and reach to counter electrode via external circuit. Meanwhile, photogenerated holes transfer from In_2O_3 to the In_2O_3/electrolyte interface and react with hydroxyl (OH^-), producing hydroxyl radical ($OH\bullet$). The $OH\bullet$ spreads to the counter electrode and reacts with electrons, completing the photogenerated carriers transport cycle. Therefore, In_2O_3 NSs PEC PDs could have self-powered photodetection capability. The self-powered PDs can transfer the light signal into an electrical signal without external power. Except for PEC PDs, the conventional solid-state PDs based on p-n or Schotty junctions also show self-powered functions. Unlike PEC PDs involving physical and chemical processes, the conventional solid-state self-powered PDs only involve physical processes, where the photogenerated carriers (electron and hole) are separated due to the built-in electric field, showing a photovoltaic effect.

Ultrathin In_2O_3 NSs show strong optical absorption in the UV region (Figure 1d), therefore, we investigated the photoresponse behavior of ultrathin In_2O_3 NSs PEC PDs irradiated by 254 nm with different bias voltages and light power intensities (Table S1, Supporting Information), as shown in **Figure 2**a. Under 254 nm irradiation, ultrathin In_2O_3 NSs PEC PDs show a typical on-off switching response. Generally, photocurrent density (J_{ph}), responsivity (R), and specific detectivity (D^*) are key parameters for quantitatively evaluating the performance of PDs, which can be calculated by the following formulas: 1) $J_{ph} = J_{light} - J_{dark}$, 2) $R = J_{ph}/P$, and 3) $D^* = R \times S^{0.5}/(2 \times q \times J_{dark} \times S + 4 \times k_b \times T/R_0)^{0.5}$, where J_{light} and J_{dark} represent the current density with and without irradiation, S, q, P, and R_0 correspond to the effective area of In_2O_3 NSs on FTO (1×1 cm^2), the quantity of electron charge (1.602×10^{-19} C), the light power intensity, and the resistance, respectively. The D^* values are calculated by considering both shot noise and thermal noise,[29,30] as shown in Tables S4 and S5, Supporting Information. At a fixed bias voltage, J_{ph} gradually increases with the increment of P due to more photogenerated carriers at stronger P. For example, J_{ph} increases from 6.86 to 10.16 µA cm^{-2} as the P increases from level I to V at a bias voltage of 0.4 V (more details in Table S2, Supporting Information). At a fixed P, the J_{ph} rapidly increases from 0 to 0.4 V, as shown in Table S2, Supporting Information. For example, J_{ph} is 0.33, 1.53, and 6.86 µA cm^{-2} for 0, 0.2, and 0.4 V at 0.04 mW cm^{-2} (level I), respectively. The J_{ph} at 0.4 V is 21-fold higher than that of 0 V (level I). Although ultrathin In_2O_3 NSs PEC PDs show a self-driven photodetection capability, J_{ph} is relatively small at 0 V (Figure S5a, Supporting Information). The J_{ph} approaches saturation at a higher bias voltage of 0.6 V, as shown in Figure S5b, Supporting Information, attributing to saturation photogeneration carriers transport at higher bias voltage. Therefore, we will focus on the performance of ultrathin In_2O_3 NSs PEC PDs at 0.4 V. Furthermore, ultrathin In_2O_3 NSs PEC PDs show good reproducibility for different devices with small deviations, as shown in Tables S2–S4, Supporting Information. As shown in Figure 2b,c, ultrathin In_2O_3 NSs PEC PDs show an outstanding photoresponse to 254 nm with an ultrahigh R of 172.36 mA W^{-1} and a remarkable D^* of 4.43×10^{11} Jones under 254 nm irradiation at 0.4 V, respectively, which surpass all recently

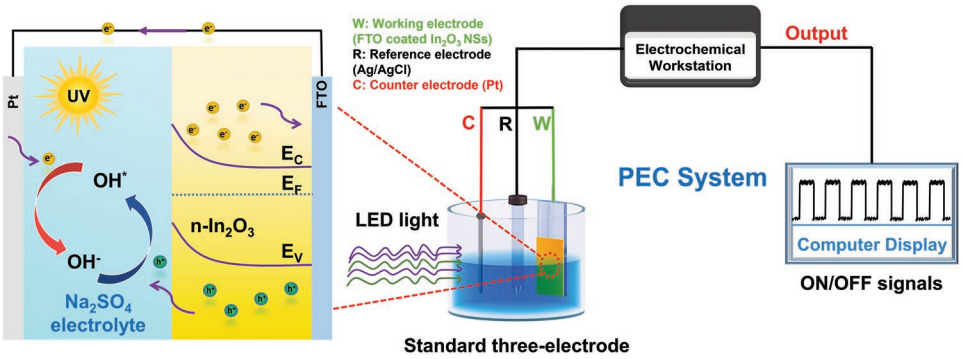

Scheme 1. Schematic diagram of evaluating ultrathin In_2O_3 NSs PEC PDs.

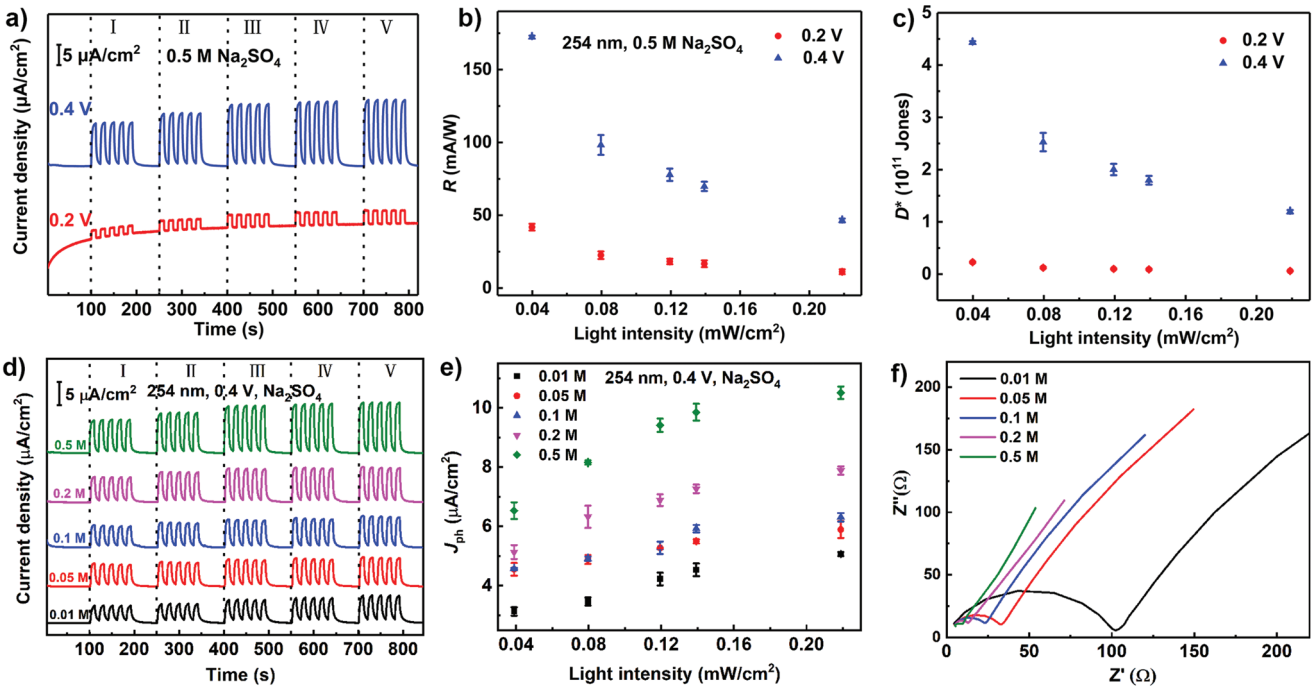

Figure 2. Photoresponse of ultrathin In_2O_3 NSs PEC PDs under 254 nm irradiation. a) *J–t* curves at various bias voltages and light power intensities (levels I, II, III, IV, and V correspond to 0.04, 0.08, 0.12, 0.14, and 0.22 mW cm^{-2}, respectively). b) Corresponding *R*. c) Corresponding *D**. d) *J–t* curves of ultrathin In_2O_3 NSs PEC PDs in various concentrations of electrolyte, including 0.01, 0.05, 0.1, 0.2, and 0.5 M Na_2SO_4. e) Corresponding J_{ph} in various concentrations of Na_2SO_4 solution. f) EIS of In_2O_3 NSs PEC PDs in different concentrations of electrolyte.

reported ultrathin nanomaterial-based aqueous-type PEC UV PDs[31–49] and are comparable with the record-high performance of recently reported PEC UV PDs,[17] as shown in Table S9, Supporting Information. The ultrahigh UV detection capability and the operation in weak alkaline electrolyte indicate that ultrathin In_2O_3 NSs hold great prospects for underwater UV communication[12] (more detailed comparison in Table S6, Supporting Information). We will focus on investigating optoelectronic properties of In_2O_3 NSs PEC PDs using seawater as the electrolyte in the future.

For PEC PDs, the electrolyte is another parameter to manipulate the photoresponse. In this study, Na_2SO_4 is chosen as the electrolyte because In_2O_3 is unstable in alkali and acid solutions. The photoresponse of ultrathin In_2O_3 NSs PEC PDs was measured in various concentrations of Na_2SO_4 solution ranging from 0.01 to 0.5 M. Ultrathin In_2O_3 NSs PEC PDs show similar on-ff switching behaviors under 254 nm irradiation in different concentrations of electrolyte, shown in Figure 2d. With increasing Na_2SO_4 concentration in the range of 0.01 – 0.5 M, J_{ph} gradually increases from 3.31 to 6.86 μA cm^{-2} at level I (Figure 2e and Table S7, Supporting Information). To further explore the mechanism of the electrolyte concentration-dependent photoresponse, we measured the electrochemical impedance spectroscopy (EIS) of ultrathin In_2O_3 NSs PEC PDs in different concentrations of Na_2SO_4 solutions, shown in Figure 2f and Table S8, Supporting Information. The R_{ct} and series resistance (R_s) reduce gradually with increasing Na_2SO_4 concentration, indicating that a higher concentration of Na_2SO_4 accelerates charge transport and facilitates photogenerated hole transfer between In_2O_3 NSs and electrolytes, leading to a higher photoresponse.

2.3. Spectral Photoresponse of Ultrathin In_2O_3 NSs PEC PDs

To understand the spectral photoresponse behavior of In_2O_3 NSs, the continuous spectral photoresponse (240–500 nm) was measured, as shown in Figure S6, Supporting Information. The photoresponse dramatically reduces as the wavelength of irradiation light increases, which is consistent with the light absorption properties. The PEC PDs show negligible photoresponse as the wavelength of irradiation light is longer than 400 nm, indicating their VBUV detection capability. To more accurately evaluate the spectral photoresponse behavior of In_2O_3 NSs, four different wavelengths of light (254, 365, 455, and 525 nm) were used to irradiate ultrathin In_2O_3 NSs PEC PDs in 0.5 M Na_2SO_4 at a fixed voltage of 0.4 V, as shown in **Figure 3**a. Obvious on-off switching signals are exhibited in the UV region (254 and 365 nm), and the J_{ph} signal rapidly declines in the visible region (455 and 525 nm). Compared with ultrathin In_2O_3 NSs, In_2O_3 NPs show a wide photoresponse region from UV to visible, as shown in Figure S7, Supporting Information. The spectral selectivity agrees well with the UV–vis absorption spectrum of ultrathin In_2O_3 NSs and commercial In_2O_3 NPs. The spectral selectivity is quantitatively evaluated by UV/visible rejection ratio ($R_{254\,nm}/R_{455\,nm}$), which are 1567 and 45.9 for ultrathin In_2O_3 NSs and In_2O_3 NPs, respectively, demonstrating the boosted spectral selectivity of ultrathin In_2O_3 NS. The spectral selectivity of ultrathin In_2O_3 NS is approximately nine and 30 times higher than those of In_2O_3 microrods[26] and commercial In_2O_3 NPs, respectively. The improved spectral selectivity is attributed to the wider bandgap of ultrathin In_2O_3 NSs originating from the quantum confinement effect.[27] The spectral

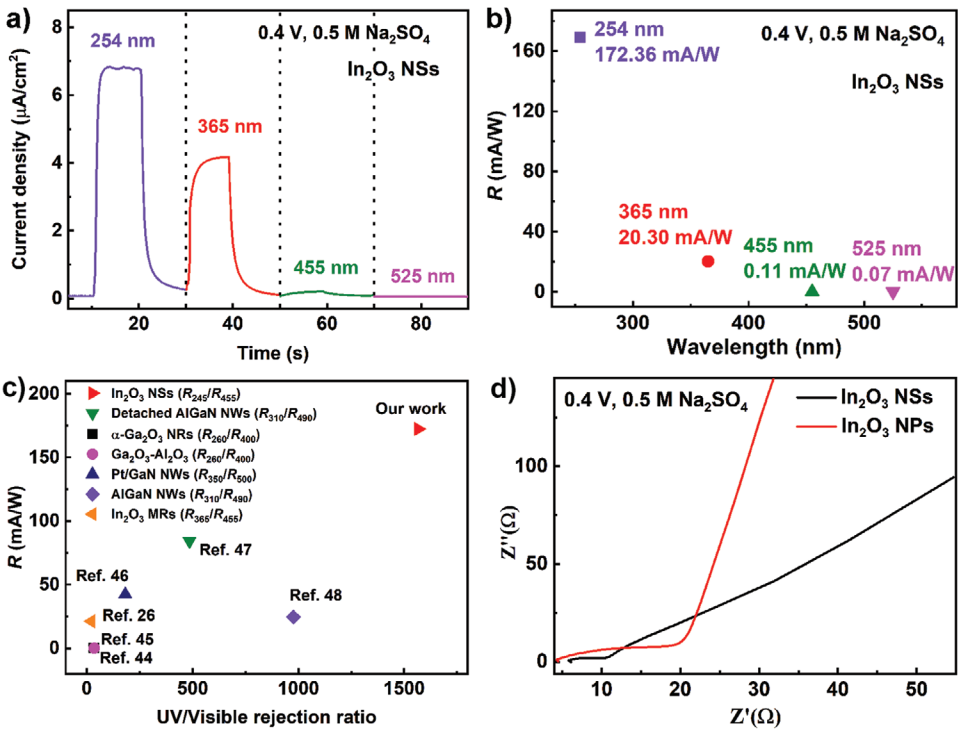

Figure 3. Spectral photoresponse of ultrathin In_2O_3 NSs PEC PDs. a) *J–t* curves of In_2O_3 NSs PEC PDs irradiated by 254, 365, 455, and 525 nm at a bias voltage of 0.4 V in 0.5 M Na_2SO_4 with a light power intensity of level I; b) corresponding *R* of In_2O_3 NSs PEC PDs irradiated by 254, 365, 455, and 525 nm; c) comparison of rejection ratios and *R* of recently reported aqueous-type PEC UV PDs. d) EIS of In_2O_3 NSs and NPs PEC PDs in 0.5 M Na_2SO_4.

selectivity and *R* of ultrathin In_2O_3 NSs PEC VBUV PDs outperform most reported aqueous-type PEC VBUV PDs,[26,44–48] as shown in Figure 3c, demonstrating their great potential in VBUV detection.

Ultrathin In_2O_3 NSs exhibit a higher photoresponse than In_2O_3 NPs in the UV region, which contradicts light absorption (Figure S3a, Supporting Information). To clarify this phenomenon, EIS of ultrathin In_2O_3 NSs and commercial In_2O_3 NPs PEC PDs in 0.5 M Na_2SO_4 solutions were recorded under 254 nm irradiation, as shown in Figure 3d. Ultrathin In_2O_3 NSs and commercial In_2O_3 NPs show almost same the fitting R_s in Table S8, Supporting Information, demonstrating their similar charge transport capability. The fitting R_{ct} of ultrathin In_2O_3 NSs is 5.797 Ω, which is 63% that of In_2O_3 NPs, demonstrating a stronger interfacial charge transfer capability at the ultrathin In_2O_3 NSs/electrolyte interface. The EIS results indicate that the higher UV photoresponse of ultrathin In_2O_3 NSs is due to easier interfacial charge transfer rather than stronger UV absorption.

2.4. Photoresponse Time and Stability of Ultrathin In_2O_3 NSs PEC PDs

The response speed and stability of ultrathin In_2O_3 NSs PEC PDs were investigated by 254 nm at 0.4 V. **Figure 4**a shows an enlarged the photo-switching cycle. The rise time (T_r) represents the time that the current rises from 10% to 90% of the maximum current, and the decay time (T_d) is the time of the maximum current reducing from 90% to 10%. The rise time (T_r) and decay time (T_d) of ultrathin In_2O_3 NSs PEC PDs are 0.8 s and 2.2 s, respectively, which are comparable to those of some aqueous-type PEC UV PDs.[26,47,49] The slower decay time is due to the persistent photoconductivity effect, which is caused by large quantity of oxygen vacancy defects and high density of trap states in metal oxide semiconductors.[50,51] The multicycle and long-term stability are key parameters for PDs in practical applications. Figure 4b shows the multicycle and long-term stability tests of In_2O_3 NSs PEC PDs in 0.5 M Na_2SO_4, which were continuously tested for 2000 s. For the fresh sample (storage for 1 month), J_{ph} decreases from 9.6 (7.4) to 8.84 (7.2) μA cm^{-2} after 2000 s, demonstrating good stability under 254 nm irradiation. The decrease in J_{ph} may be due to decomposition of nanocrystals or pilling-off from the substrate. Ultrathin In_2O_3 PEC PDs exhibit good multicycle and long-term stability, which are superior to most aqueous-type ultrathin nanomaterial-based PEC UV PDs.[31–43]

2.5. Imaging Capability of Ultrathin In_2O_3 NSs PEC PDs

To further verify the capability of our devices for underwater imaging applications, the ultrathin In_2O_3 NSs PEC PDs are employed in a single-pixel imaging system. As shown in **Figure 5**a, the imaging system consists of a hollow plate with the school badge (Northeast Forestry University), a laser light source (375 nm, 0.06 mW cm^{-2}), a source meter (Keithley 6482), an oscilloscope, and a computer. The object is mounted on a computer-controlled X-Y platform so that it can move continuously and stably in both horizontal and vertical directions,

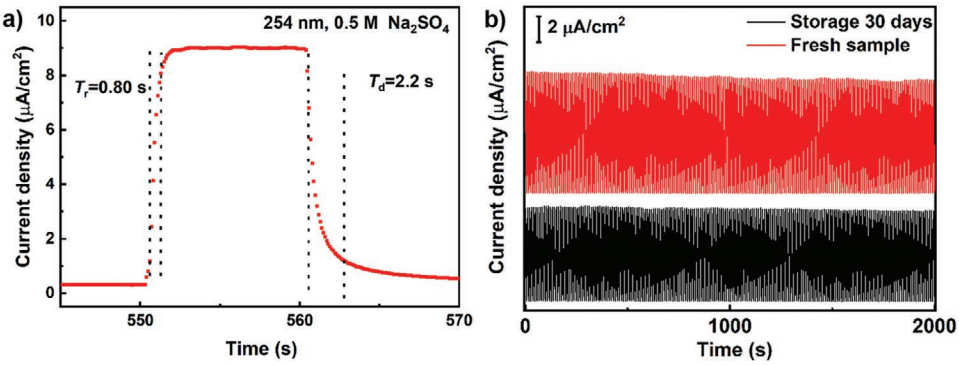

Figure 4. Photoresponse time and stability of ultrathin In_2O_3 NSs PEC PDs. a) Amplified photo-switching cycle irradiated by 254 nm (Level III) in 0.5 M Na_2SO_4. b) Stability measurements of fresh samples and storage for 1 month for 2000 s (light on 5 s and light off 5 s).

and the current signals are collected by the source meter at the same time. A 103 × 103 pixels image is obtained under the bias of 0.4 V, as shown in Figure 5b. The clear and accurate pattern of the school badge proves the underwater imaging capability of the device. Figure 5c shows the profile of the red line in Figure 5b, and the rapid increases and decreases of signal intensity prove the device's reliability when applied to underwater imaging. The imaging process can also be achieved in a self-powered mode. As shown in Figure S8, Supporting Information, limited by ambient noise and instrument accuracy, the image obtained in self-powered mode is slightly worse but can be distinguished. These imaging results demonstrate the potential application capabilities of ultrathin In_2O_3 NSs PEC PDs.

3. Conclusion

In summary, we first demonstrated that individual ultrathin In_2O_3 NSs have great potential in high-performance PEC VBUV PDs with high responsivity and excellent spectral

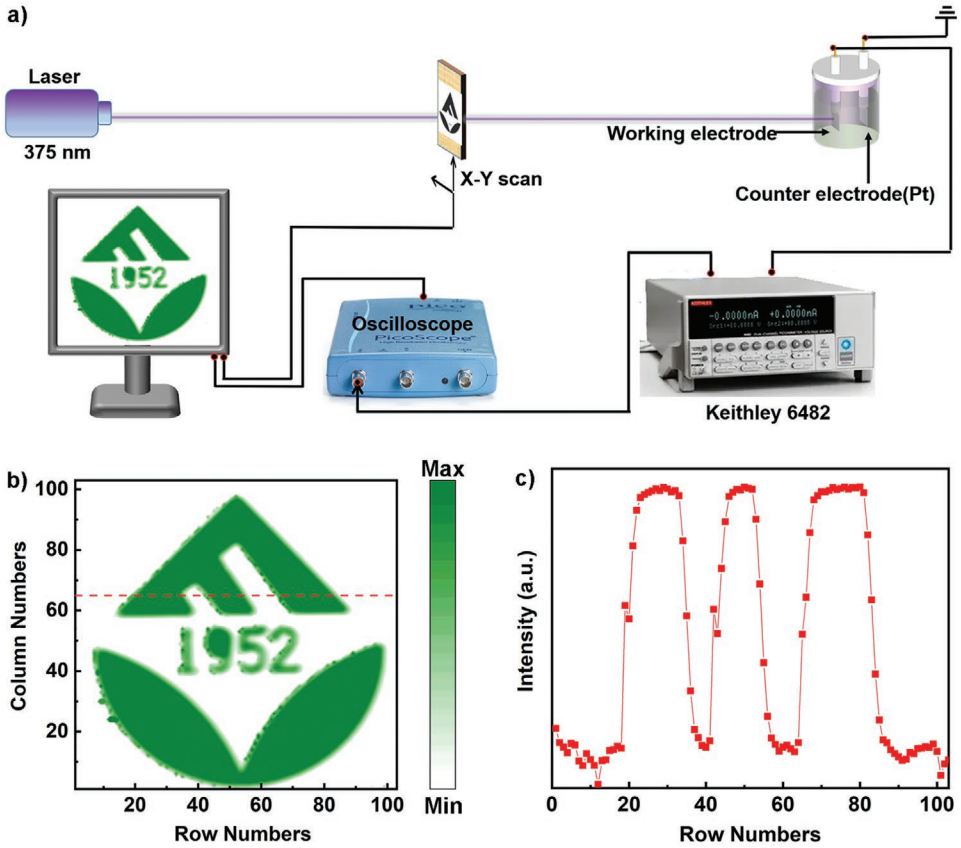

Figure 5. Imaging Capability of ultrathin In_2O_3 NSs PEC PDs. a) Schematic diagram of the imaging system. b) Imaging under a bias of 0.4 V. c) Detected signal along the red line in (b).

selectivity. Ultrathin In_2O_3 NSs PEC PDs show excellent UV photodetection with an ultrahigh R of 172.36 mA W^{-1} and a remarkable D^* of 4.43×10^{11} Jones under 254 nm irradiation. The outstanding UV photoresponse originates from the smaller charge transfer resistance at the ultrathin In_2O_3 NSs/electrolyte interface. Furthermore, the light absorption of ultrathin In_2O_3 NSs takes a blueshift due to the quantum confinement effect, granting ultrathin In_2O_3 NSs PEC PDs good spectral selectivity for visible-blind detection. The UV–visible rejection ratio of In_2O_3 NSs PEC PDs is 1567, which exceeds all recently reported PEC VBUV PDs. Moreover, ultrathin In_2O_3 NSs PEC PDs show good multicycle and long-term stability under 254 nm irradiation. Furthermore, In_2O_3 NSs PEC PDs show good underwater imaging capability under UV irradiation. Our results demonstrate that ultrathin In_2O_3 NSs are good candidates for high-performance VBUV PDs.

4. Experimental Section

Photoresponse Activity: In brief, In_2O_3 (2 mg) NSs/NPs were dispersed into 1 mL of PVDF/DMF (2 mg/10 mL) by sonicating for 60 min. The mixture was then directly dropped onto the conductive side of FTO glass, and the In_2O_3-coated FTO (effective area of In_2O_3 NSs on FTO was 1×1 cm^2) was dried in a vacuum drying oven at 80 °C for 12 h. The electrical characterization was carried out in a three-electrode system using a CHI660E electrochemical workstation (Chenhua Instrument Company, China). In_2O_3 NSs/NPs-coated FTO glass, Pt wire, and Ag/AgCl electrodes were used as the working electrode, counter electrode, and reference electrode, respectively. The photodetection performance was investigated in different concentrations of Na_2SO_4 (0.01, 0.05, 0.1, 0.2, and 0.5 M) with different wavelengths of light (254, 365, 455, and 525 nm). The electrochemical impedance spectrum (EIS) was determined in a frequency range of 0.01 Hz–10^5 Hz with a perturbation amplitude of 0.005 V. Measurements of continuous spectral responsivity were performed using a Zolix DR800-CUST and a CHI660E electrochemical workstation. A monochromatic light with a continuously tunable wavelength (200–500 nm) illuminated the sample surface, and the generated photocurrents from the In_2O_3 NSs PEC PDs were collected by the electrochemical workstation. After testing, the light intensity of monochromatic light was measured with the optical power meter (ThorLabs, PM120VA). The imaging system consisted of a hollow plate with the school badge (Northeast Forestry University), a laser light source (375 nm, 0.06 mW cm^{-2}), a source meter (Keithley 6482), an oscilloscope, and a computer. The school badge was mounted on a computer-controlled X-Y platform. A 103×103 pixels image was obtained under the bias of 0 and 0.4 V.

Statistical Analysis: Statistical analyses were conducted using OriginPro 2018 (OriginLab Software, Northampton, Massachusetts, USA). Data from photocurrent density, responsivity, and specific detectivity of In_2O_3 NSs PEC PDs irradiated by 254 nm with different power intensities were calculated and processed as mean ± standard deviation (SD). The error bars were based on the SD of the mean.

Supporting Information

Supporting Information is available from the Wiley Online Library or from the author.

Acknowledgements

M.Z., H.Y., and H.L. contributed equally to this work. The authors gratefully acknowledge the support from the Heilongjiang Provincial Natural Science Foundation of China (no. YQ2020E003) and the Fundamental Research Funds for the Central Universities (no. 2572021BU01).

Conflict of Interest

The authors declare no conflict of interest.

Data Availability Statement

The data that support the findings of this study are available from the corresponding author upon reasonable request.

Keywords

In_2O_3, nanosheets, photodetectors, photoelectrochemical, visible-blind

Received: September 12, 2022
Revised: October 28, 2022
Published online: November 13, 2022

[1] C. Xie, X.-T. Lu, X.-W. Tong, Z.-X. Zhang, F.-X. Liang, L. Liang, L.-B. Luo, Y.-C. Wu, *Adv. Funct. Mater.* **2019**, *29*, 1806006.
[2] A. Rogalski, J. Antoszewski, L. Faraone, *J. Appl. Phys.* **2009**, *105*, 091101.
[3] J. Chen, W. Ouyang, W. Yang, J.-H. He, X. Fang, *Adv. Funct. Mater.* **2020**, *30*, 1909909.
[4] Y. Yan, J. Yang, J. Du, X. Zhang, Y.-Y. Liu, C. Xia, Z. Wei, *Adv. Mater.* **2021**, *33*, 2008761.
[5] Y. Ping, H. Long, H. Liu, C. Chen, N. Zhang, H. Jing, J. Lu, Y. Zhao, Z. Yang, W. Li, F. Ma, X. Fang, Z. Wei, H. Xu, *Adv. Funct. Mater.* **2022**, *32*, 2111673.
[6] W. Yang, K. Xin, J. Yang, Q. Xu, C. Shan, Z. Wei, *Small Methods* **2022**, *6*, 2101348.
[7] Y. Yu, T. Shen, H. Long, M. Zhong, K. Xin, Z. Zhou, X. Wang, Y.-Y. Liu, H. Wakabayashi, L. Liu, J. Yang, Z. Wei, H.-X. Deng, *Adv. Mater.* **2022**, *34*, 2206486.
[8] M. Long, P. Wang, H. Fang, W. Hu, *Adv. Funct. Mater.* **2019**, *29*, 1803807.
[9] L. Peng, L. Hu, X. Fang, *Adv. Mater.* **2013**, *25*, 5321.
[10] J. Han, F. Wang, S. Han, W. Deng, X. Du, H. Yu, J. Gou, Q. J. Wang, J. Wang, *Adv. Funct. Mater.* **2022**, *32*, 2205150.
[11] J. Zhou, L. Chen, Y. Wang, Y. He, X. Pan, E. Xie, *Nanoscale* **2016**, *8*, 50.
[12] Y. Luo, D. Wang, Y. Kang, X. Liu, S. Fang, M. H. Memon, H. Yu, H. Zhang, D. Luo, X. Sun, B. S. Ooi, C. Gong, Z. Xu, H. Sun, *Adv. Opt. Mater.* **2022**, *10*, 2102839.
[13] X. Li, C. Gao, H. Duan, B. Lu, X. Pan, E. Xie, *Nano Energy* **2012**, *1*, 640.
[14] K. Chen, S. Wang, C. He, H. Zhu, H. Zhao, D. Guo, Z. Chen, J. Shen, P. Li, A. Liu, C. Li, F. Wu, W. Tang, *ACS Appl. Nano Mater.* **2019**, *2*, 6169.
[15] X. Hou, X. Wang, B. Liu, Q. Wang, Z. Wang, D. Chen, G. Shen, *ChemElectroChem* **2014**, *1*, 108.
[16] D. Wang, X. Liu, S. Fang, C. Huang, Y. Kang, H. Yu, Z. Liu, H. Zhang, R. Long, Y. Xiong, Y. Lin, Y. Yue, B. Ge, T. K. Ng, B. S. Ooi, Z. Mi, J.-H. He, H. Sun, *Nano Lett.* **2021**, *21*, 120.
[17] X. Liu, D. Wang, P. Shao, H. Sun, S. Fang, Y. Kang, K. Liang, H. Jia, Y. Luo, J. Xue, J. Wang, T. Zhi, D. Chen, B. Liu, S. Long, R. Zhang, *Adv. Funct. Mater.* **2022**, *32*, 2201604.

[18] Y. Kang, D. Wang, S. Fang, X. Liu, H. Yu, H. Jia, H. Zhang, Y. Luo, B. S. Ooi, J.-H. He, H. Sun, S. Long, *ACS Appl. Nano Mater.* **2021**, *4*, 13938.
[19] X. Li, C. Gao, H. Duan, B. Lu, Y. Wang, L. Chen, Z. Zhang, X. Pan, E. Xie, *Small* **2013**, *9*, 2005.
[20] D. Ni, Y. Wang, A. Li, L. Huang, H. Tang, B. Liu, C. Cheng, *Nanoscale* **2022**, *14*, 3159.
[21] M. Meng, X. Wu, X. Ji, Z. Gan, L. Liu, J. Shen, P. K. Chu, *Nano Res.* **2017**, *10*, 2772.
[22] R. L. Weiher, R. P. Ley, *J. Appl. Phys.* **1966**, *37*, 299.
[23] A. D. Mottram, Y.-H. Lin, P. Pattanasattayavong, K. Zhao, A. Amassian, T. D. Anthopoulos, *ACS Appl. Mater. Interfaces* **2016**, *8*, 4894.
[24] V. Kumar, S. M. Majhi, K.-H. Kim, H. W. Kim, E. E. Kwon, *Chem. Eng. J.* **2021**, *404*, 126472.
[25] D. Shao, L. Qin, S. Sawyer, *Appl. Surf. Sci.* **2012**, *261*, 123.
[26] M. Cui, Z. Shao, L. Qu, X. Liu, H. Yu, Y. Wang, Y. Zhang, Z. Fu, Y. Huang, W. Feng, *ACS Appl. Mater. Interfaces* **2022**, *14*, 39046.
[27] J. G. Labram, N. D. Treat, Y.-H. Lin, C. H. Burgess, M. A. McLachlan, T. D. Anthopoulos, *Adv. Funct. Mater.* **2016**, *26*, 1656.
[28] X. Wang, J. Su, H. Chen, G.-D. Li, Z. Shi, H. Zou, X. Zou, *ACS Appl. Mater. Interfaces* **2017**, *9*, 16335.
[29] Y. Chen, Y. Wang, Z. Wang, Y. Gu, Y. Ye, X. Chai, J. Ye, Y. Chen, R. Xie, Y. Zhou, Z. Hu, Q. Li, L. Zhang, F. Wang, P. Wang, J. Miao, J. Wang, X. Chen, W. Lu, P. Zhou, W. Hu, *Nat. Electron.* **2021**, *4*, 357.
[30] P. Wu, L. Ye, L. Tong, P. Wang, Y. Wang, H. Wang, H. Ge, Z. Wang, Y. Gu, K. Zhang, Y. Yu, M. Peng, F. Wang, M. Huang, P. Zhou, W. Hu, *Light: Sci. Appl.* **2022**, *11*, 6.
[31] W. Huang, C. Xing, Y. Wang, Z. Li, L. Wu, D. Ma, X. Dai, Y. Xiang, J. Li, D. Fan, H. Zhang, *Nanoscale* **2018**, *10*, 2404.
[32] T. Fan, Z. Xie, W. Huang, Z. Li, H. Zhang, *Nanotechnology* **2019**, *30*, 114002.
[33] M. I. Zappia, G. Bianca, S. Bellani, M. Serri, L. Najafi, R. Oropesa-Nuñez, B. Martín-García, D. Bouša, D. Sedmidubský, V. Pellegrini, Z. Sofer, A. Cupolillo, F. Bonaccorso, *Adv. Funct. Mater.* **2020**, *30*, 1909572.
[34] L. Gao, H. Chen, R. Wang, S. Wei, A. V. Kuklin, S. Mei, F. Zhang, Y. Zhang, X. Jiang, Z. Luo, S. Xu, H. Zhang, H. Ågren, *Small* **2021**, *17*, 2005913.
[35] L. Gao, R. Wang, A. V. Kuklin, H. Zhang, H. Ågren, *Adv. Funct. Mater.* **2021**, *31*, 2010401.
[36] C. Xing, W. Huang, Z. Xie, J. Zhao, D. Ma, T. Fan, W. Liang, Y. Ge, B. Dong, J. Li, H. Zhang, *ACS Photonics* **2018**, *5*, 621.
[37] Y. Zhang, P. Huang, J. Guo, R. Shi, W. Huang, Z. Shi, L. Wu, F. Zhang, L. Gao, C. Li, X. Zhang, J. Xu, H. Zhang, *Adv. Mater.* **2020**, *32*, 2001082.
[38] C. Xing, X. Chen, W. Huang, Y. Song, J. Li, S. Chen, Y. Zhou, B. Dong, D. Fan, X. Zhu, H. Zhang, *ACS Photonics* **2018**, *5*, 5055.
[39] D. Ma, J. Zhao, R. Wang, C. Xing, Z. Li, W. Huang, X. Jiang, Z. Guo, Z. Luo, Y. Li, J. Li, S. Luo, Y. Zhang, H. Zhang, *ACS Appl. Mater. Interfaces* **2019**, *11*, 4278.
[40] Z. Xie, C. Xing, W. Huang, T. Fan, Z. Li, J. Zhao, Y. Xiang, Z. Guo, J. Li, Z. Yang, B. Dong, J. Qu, D. Fan, H. Zhang, *Adv. Funct. Mater.* **2018**, *28*, 1705833.
[41] D. Ma, R. Wang, J. Zhao, Q. Chen, L. Wu, D. Li, L. Su, X. Jiang, Z. Luo, Y. Ge, J. Li, Y. Zhang, H. Zhang, *Nanoscale* **2020**, *12*, 5313.
[42] M. I. Zappia, G. Bianca, S. Bellani, N. Curreli, Z. Sofer, M. Serri, L. Najafi, M. Piccinni, R. Oropesa-Nuñez, P. Marvan, V. Pellegrini, I. Kriegel, M. Prato, A. Cupolillo, F. Bonaccorso, *J. Phys. Chem. C* **2021**, *125*, 11857.
[43] X. Yang, X. Liu, L. Qu, F. Gao, Y. Xu, M. Cui, H. Yu, Y. Wang, P. Hu, W. Feng, *ACS Nano* **2022**, *16*, 8440.
[44] J. Zhang, S. Jiao, D. Wang, S. Ni, S. Gao, J. Wang, *J. Mater. Chem. C* **2019**, *7*, 6867.
[45] J. Zhang, S. Jiao, D. Wang, S. Gao, J. Wang, L. Zhao, *Appl. Surf. Sci.* **2021**, *541*, 148380.
[46] S. Fang, D. Wang, X. Wang, X. Liu, Y. Kang, H. Yu, H. Zhang, W. Hu, J.-H. He, H. Sun, S. Long, *Adv. Funct. Mater.* **2021**, *31*, 2103007.
[47] M. Jiang, Y. Zhao, L. Bian, W. Yang, J. Zhang, Y. Wu, M. Zhou, S. Lu, H. Qin, *ACS Photonics* **2021**, *8*, 3282.
[48] M. Jiang, J. Zhang, W. Yang, D. Wu, Y. Zhao, Y. Wu, M. Zhou, S. Lu, *Adv. Mater. Interfaces* **2022**, *9*, 2200028.
[49] C. He, D. Guo, K. Chen, S. Wang, J. Shen, N. Zhao, A. Liu, Y. Zheng, P. Li, Z. Wu, C. Li, F. Wu, W. Tang, *ACS Appl. Nano Mater.* **2019**, *2*, 4095.
[50] S. Jeon, S.-E. Ahn, I. Song, C. J. Kim, U. I. Chung, E. Lee, I. Yoo, A. Nathan, S. Lee, K. Ghaffarzadeh, J. Robertson, K. Kim, *Nat. Mater.* **2012**, *11*, 301.
[51] Z. Han, H. Liang, W. Huo, X. Zhu, X. Du, Z. Mei, *Adv. Opt. Mater.* **2020**, *8*, 1901833.

